

Laser-Induced Transformation of ZIF-8 into Highly Luminescent N-Doped Nanocarbons for Flexible Sensors

Tuan-Hoang Tran, Aura Garcia, Dmitry Kogolev, Pavel S. Postnikov, Ranran Wang,*
Raul D. Rodriguez,* and Evgeniya Sheremet

Metal–organic frameworks (MOFs) like the zeolitic imidazolate framework (ZIF-8) have a high surface area, tunable porosity, and robust thermal and chemical stability, making them attractive candidates for various applications. Here, a strategy is shown that spans that functionality and provides strong photoluminescence (PL) emission, unlocking ZIF-8-based materials for chemical and temperature sensors based on PL. The approach is based on laser processing that dramatically boosts the PL response of laser-irradiated ZIF-8 (LI ZIF-8), achieving a 70-fold increase in intensity relative to the pristine material. The PL characteristics of the irradiated material can be easily tuned by varying the laser power and irradiation time with in situ and real-time spectroscopic analysis providing insights into the process dynamics. It is found that the observed PL enhancement is primarily due to the laser-induced transformation of ZIF-8 into nitrogen-doped nanocarbons and ZnO nanostructures. The versatility of this laser processing approach is leveraged to create flexible electronics by integrating the LI ZIF-8/nanocarbon architectures into thermoplastic polyurethane (TPU). The multifunctional composite material shows excellent performance as flexible electrodes for human-body monitoring applications, as well as both temperature and flexure sensors with remarkable mechanical resilience.

1. Introduction

The emergence of flexible electronics is a significant technological breakthrough of the 21st century, revolutionizing how we interact with electronics and opening a new dimension for portable devices. This technological field offers high adaptability so that electronic devices can be gradually integrated into

flexible and lightweight surfaces. The development of the Internet of Things (IoT) further emphasizes the importance of flexible sensors capable of continuously tracking various signals such as temperature, pressure, and bending angle. These technologies occupy a crucial role in health monitoring systems. In these systems, the commonly used nanomaterials are carbon-based materials,^[1] Mxenes,^[2] and conductive polymers.^[3] Most recently, metal–organic frameworks (MOFs) have been explored for wearable sensors thanks to their valuable properties: large surface area, controllable porosity, and a wide range of combinations of metal ions and organic ligands.^[4] These properties have continuously attracted the attention of both academic and industrial communities. Although MOFs have wide versatility, one limitation when developing sensing platforms is their relatively low luminescence intensity. Several strategies have been designed to increase the luminescence of MOFs, such as adding carbon quantum

dots (CQDs) to their ligands,^[5] encapsulating quantum dots in their structure,^[6] or by calcination.^[7] For instance, incorporating carbon dots with high quantum yield into the MOFs during synthesis increases the luminescence properties, making MOFs more effective for chemical sensing applications.^[8] Additionally, CQDs within the MOF structure improve charge carrier separation and light absorption in the visible region, leading to higher photocatalytic activity with a better performance in the reduction of Cr(VI) to Cr(III).^[9] The ability to confine ultra-small quantum dots using MOF structures as templates has been demonstrated from CdSe^[10] to perovskites,^[11] offering potential applications in photocatalysis and solar cells. However, these methods often require considerable energy consumption, complex synthesis steps, and time-consuming procedures.

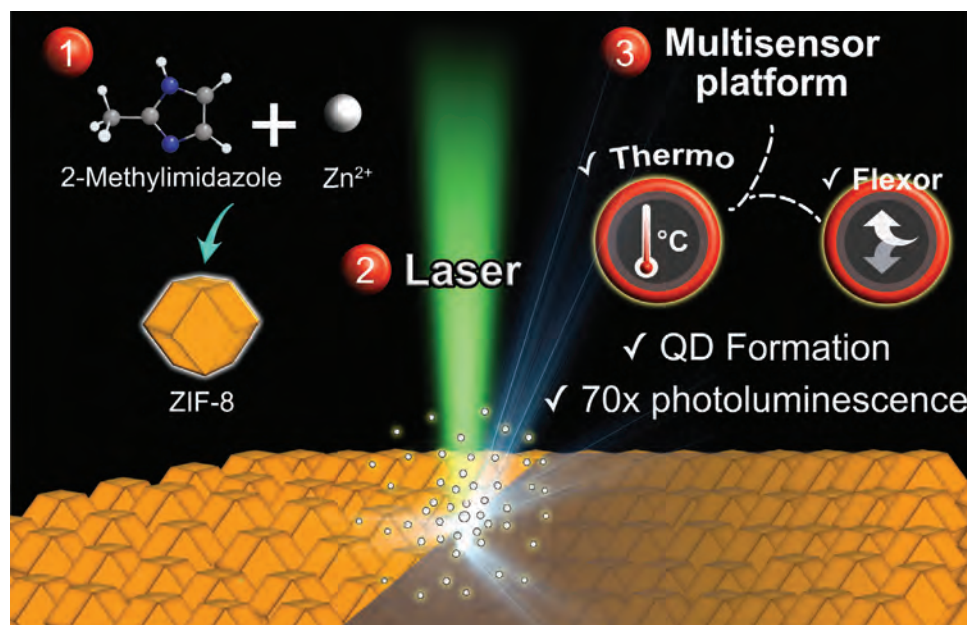
An alternative, more efficient approach to modifying the luminescence properties of materials is laser processing. This technique can induce localized photothermal and photochemical effects and structural changes.^[12–14] While lasers are being used in the microfabrication of sensors, their potential to alter MOFs' luminescence has not yet been explored. This work presents an innovative laser-based approach to transform MOF into highly luminescent N-doped nanocarbons. This research focuses on a subclass of MOFs, specifically those based on Zn ions and

T.-H. Tran, A. Garcia, D. Kogolev, P. S. Postnikov, R. D. Rodriguez,
E. Sheremet
Tomsk Polytechnic University
Lenina avenue, 30, Tomsk 634050, Russia
E-mail: raul@tpu.ru

R. Wang
The State Key Lab of High Performance Ceramics and Superfine
Microstructure
Shanghai Institute of Ceramics
Chinese Academy of Sciences
Shanghai 200050, China
E-mail: wangranran@mail.sic.ac.cn

The ORCID identification number(s) for the author(s) of this article can be found under <https://doi.org/10.1002/adom.202401758>

DOI: 10.1002/adom.202401758



Scheme 1. Graphical representation of the laser-induced transformation of ZIF-8 to nitrogen-doped nanocarbons, highlighting the resultant quantum dot formation and the up to 40-fold increase in photoluminescence, leading to a versatile multisensor platform for temperature and flexural sensing.

imidazolate ligands, known as Zeolitic Imidazolate Frameworks (ZIF-8). ZIF-8 is renowned for its easy preparation, high porosity, and exceptional thermal and chemical stability (Scheme 1).^[15]

Our laser treatment approach allows the integration of the laser-irradiated ZIF-8 (LI ZIF-8) into flexible thermoplastic polyurethane (TPU), leading to the development of electrodes suitable for wearable sensors. The resulting composite uniquely combines biomechanical compliance with sensitivity of photoemission to temperature and electrical resistance to mechanical strain. Given the prevalence of TPU in medical applications, we take advantage of such multifunctionality to showcase proof-of-concept applications in temperature monitoring and bending sensors. Our scalable approach to converting MOFs into tailored luminescent nanocarbons integrated into biocompatible polymers paves the way for the forthcoming generation of flexible electronics.

2. Results and Discussion

2.1. Emergence of PL in Laser-Treated ZIF-8 at the Micro-Scale

These experiments aimed to establish the impact of continuous-wave laser irradiation on the photoluminescence (PL) properties of ZIF-8 and do this while in situ recording the spectroscopic changes of the material using Raman spectroscopy. The motivation for this approach is that we expected structural, physical, and chemical changes induced by the laser in the Raman microscope while spectroscopically monitoring those changes in real time in a single experiment. From the most common laser lines used in Raman microscopy (NIR, red, green, and blue), we selected the blue laser at 457 nm since the absorption of ZIF-8 and ligand 2-methylimidazole is higher for the blue spectral range as compared to the other wavelengths (Figure S1, Supporting Informa-

tion). Choosing the 457 nm laser implies less power is needed to process ZIF-8.

Under these conditions, we selectively irradiated ZIF-8 films deposited on glass slides (Figure 1a inset). Initially, a PL map was captured at a low laser power (1 μ W) to evaluate the ZIF-8's inherent luminescence without inducing changes in the material. These results are presented in Figure 1a, revealing a uniform PL distribution.

To observe in real-time the PL evolution under laser exposure, we increased the laser power over 4000 times (to 4.1 mW), focused on a single spot on the sample surface, and recorded the time-resolved PL emission (Figure 1b). One of the most exciting observations from these experiments was the strong PL enhancement that peaked at 2.5 s before rapidly declining. Repeated experiments confirmed the reproducibility of this result across both uniform and nonuniform ZIF-8 films (see Figure S2, Supporting Information). Although the final PL decrease is an indication of ZIF-8's ablation, we wondered what happened to the material before it was ablated. In particular, we wanted to determine if we could control the ZIF-8 irradiation to freeze the resulting material in a state with high PL emissions.

First, it was necessary to elucidate the mechanism behind the PL enhancement. For this, we investigated time-series PL spectra from a single irradiation point captured at different intervals (Figure 1c). At the outset (0.06 s), conventional ZIF-8 Raman peaks were observed in addition to a negligible PL emission. At the 2.5-s mark, a sudden rise in PL intensity was observed, which then decreased after 2.6 s. Spatial PL mapping around this zone revealed an interesting pattern: a large increase in PL surrounding the irradiated area compared to both the ablated core and non-irradiated regions (Figure 1d). The PL spectra in Figure 1e were extracted from the spectral profile along the white dashed line in Figure 1d. As we can see, the spatial PL behavior across the ablated spot showed not only an amplified PL intensity but

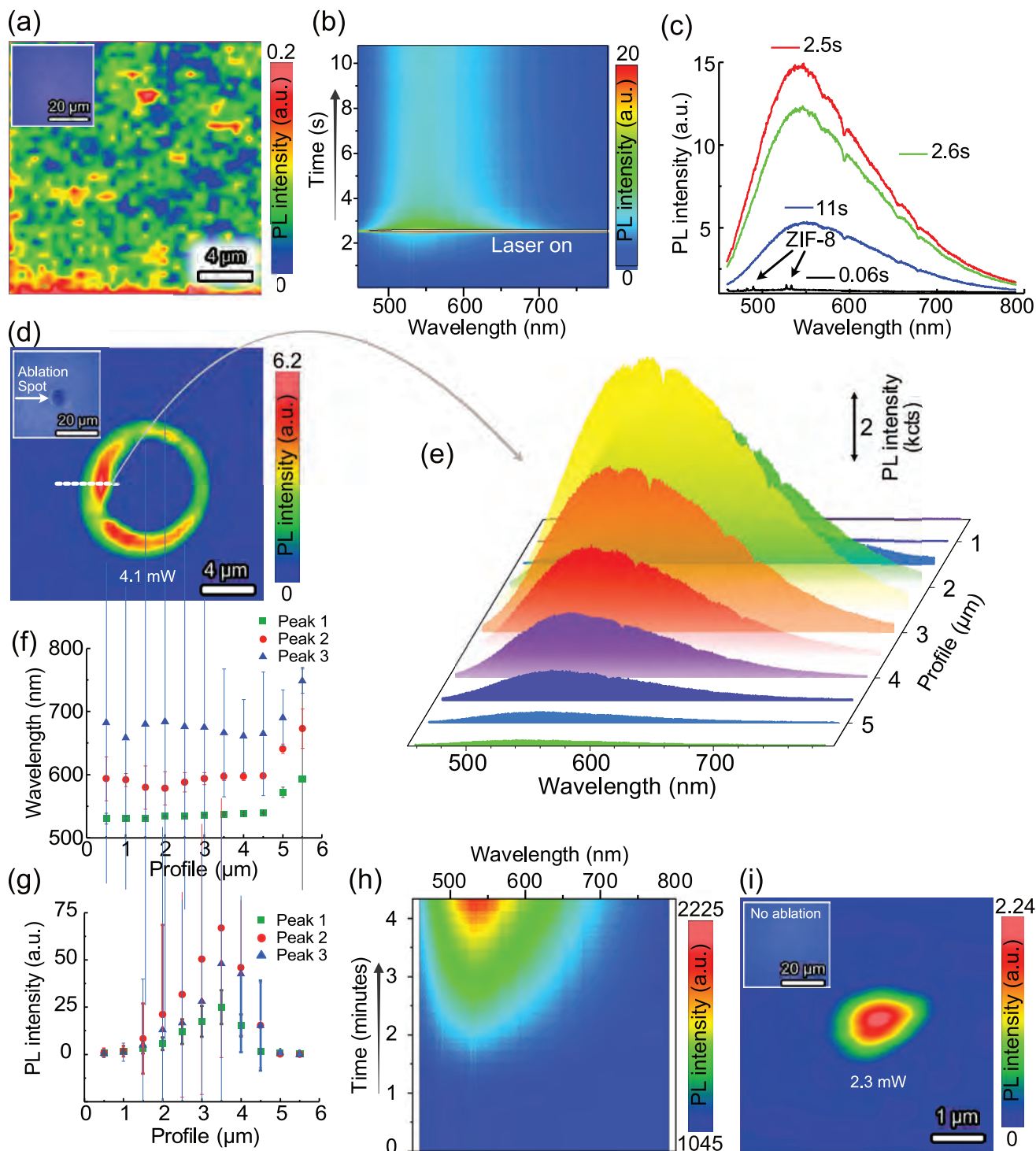


Figure 1. Laser treatment of ZIF-8 in microscale. a) PL intensity map of ZIF-8 before laser treatment (Inset: Optical image of ZIF-8). b) Time-resolved PL emission spectra of ZIF-8 during laser treatment. c) PL spectra at 0.06, 2.5, 2.6, and 11 s irradiation time. d) Spatial dependence PL intensity map after laser ablation (inset: optical image of ZIF-8 after laser treatment). e) PL spectra, extracted from the spectral profile along the white dashed line in Figure 1d. f) Peak intensity of 3 distinct emission bands at ≈ 530 , 590, and 680 nm. g) Peak position of three PL peaks fitted by Gaussian distributions from the profile. h) Time-resolved PL emission spectra of ZIF-8 during laser treatment with smaller laser power to not induce ablation. i) Spatial PL map after laser treatment of ZIF-8 without ablation (inset: an optical image of ZIF-8 after laser treatment without ablation).

also a shift in the PL peak emission wavelength. After fitting the PL spectra with Gaussian distribution functions (Figure S3, Supporting Information), we found three distinct emission bands at ≈ 530 , 590, and 680 nm. These bands appeared red-shifted compared to pristine ZIF-8 (Figure 1f). The PL intensity of all three peaks revealed the same behavior as they both increased from the unirradiated region to the region around the irradiated spot and then suddenly dropped. The PL intensity's spatial profile evidenced a significant 70-fold amplification near the ablation point (Figure 1g).

Interestingly, PL enhancement occurred even in ZIF-8 regions beyond the ablation zone, with variable PL peak wavelengths. This observation suggests the potential for PL tuning via laser power and duration without involving material ablation. To further investigate this point, we conducted analogous experiments at reduced power levels to 2.38 mW under a 100x objective, achieving PL enhancement without visible material changes, as deduced by optical microscopy. These findings, depicted in the time-dependent PL spectra in Figure 1h and the high-resolution spatial PL map in Figure 1i, confirm that laser treatment boosted PL without ablating ZIF-8 (also compare optical microscopy images in Figure 1d vs Figure 1i insets). The PL temporal evolution in Figure 1h reveals increased emission intensity over time.

Understanding the mechanisms behind PL enhancement is critical for elucidating the effects of laser treatment on ZIF-8. We hypothesize that the observed PL enhancement results from laser-induced transformations are analogous to the photothermal effects reported in recent studies on MoS₂ flakes.^[18] In ambient conditions, the laser's focal point generates localized heating within ZIF-8, with thermal diffusion raising the temperature in areas around. Such heat increase could lead to the transformation of ZIF-8 into either a luminescent carbon matrix and/or ZnO nanoparticles.^[19] The possibility of PL emission by ZnO could be overruled considering the mismatch between the laser excitation energy and bulk ZnO's band gap (3.3 eV).^[20] This band gap increases with reduced nanoparticle size due to quantum confinement effects.^[21] However, defect states could introduce energy levels inside the ZnO band gap that could be accessed via the blue laser (2.71 eV) used in our experiments.^[22,23] Consequently, the PL emission can be attributed to the formation of carbon-based nanostructures and/or ZnO nanoparticles within ZIF-8. The presence of carbon structures was confirmed by the D and G band signatures in the PL background (Figure S2d, Supporting Information), which can originate from the organic 2-methylimidazole linker that forms sp²-bonded carbon nanodots during laser irradiation.^[7] Control experiments with 2-methylimidazole alone also showed PL enhancement, although requiring much higher laser power (10 mW) and resulting in a smaller ablation site (Figure S4, Supporting Information). This result highlights the linker's lower absorbance relative to ZIF-8 (Figure S1, Supporting Information). Attempts to induce ablation with a green laser were unsuccessful due to the low absorbance of both materials at 532 nm. These observations led us to propose the following conversion mechanism from ZIF-8 to nanocarbons by laser irradiation: First, ZIF-8 is photothermally heated by laser treatment. When the temperature reaches a threshold value, 2-methylimidazole transforms into nanocarbons. As the temperature increases, more 2-methylimidazole is converted to nanocarbons, consequently increasing the PL intensity. At higher tem-

peratures, the 2-methylimidazole becomes "over carbonized,"^[7] i.e., the nanocarbon's size becomes larger. These results agree with the literature; for instance, Reyes and coauthors showed that their material's PL emission decreased as the size of CDNs increased.^[24] In the center of the laser-irradiated spot, where the temperature is the highest, 2-methylimidazole is partially removed due to ablation and burning; these two processes decrease PL. Due to focused laser irradiation, a highly localized heating effect occurs, resulting in high temperatures at the laser spot's center. Heat transfer causes a radial decrease in temperature away from the irradiated spot. Consequently, the PL intensity diminishes, and the emission wavelength exhibits a blue shift as the distance from the ablated spot increases. Wang et al.^[7] demonstrated that high-temperature calcination of ZIF-8 promotes the generation of carbon nanodots from the 2-methylimidazole linker, thereby boosting PL. They observed that increased calcination duration at 200 °C first increased the PL to a peak value at 5 h before a subsequent intensity decrease. The redshift observed in the PL spectra is likely due to localized thermal effects, which, with rising temperatures, increase the size of carbon nanodots, the prevalence of graphene oxide quantum dots, or the nitrogen content within the dots, all factors that contribute to the shift in PL emission.^[25–28] In contrast to Wang et al. work, our laser processing approach achieves the spatial transformation of ZIF-8 into luminescent nanocarbons with resolutions down to the microscale, requiring less intensive processing than thermal annealing making it compatible with temperature-sensitive materials and doing this at a fraction of the time.

As mentioned above, the PL intensity is not homogeneous due to the inhomogeneous temperature induced by laser treatment, which may lead to different quality of nanocarbons. Unfortunately, as shown in Figure S5 (Supporting Information), the high PL emission prevents us from observing the characteristic D and G Raman peaks.

2.2. Macroscale LI-ZIF-8 on Glass

The preceding analysis demonstrated the feasibility of transforming ZIF-8 into highly luminescent nanocarbons and defected ZnO nanoparticles using a tightly focused laser in a Raman microscope. To show the scalability of this approach, we implemented a computer-controlled 450 nm laser station to carry out large-area laser processing of ZIF-8 films on glass.

The LI ZIF-8 morphology was observed via scanning electron microscopy (SEM), as depicted in Figure 2a, revealing extensions of microporous regions resembling both flatlands and islands after irradiation. These island-like structures, formed under high laser intensity, had a porous surface texture (Figure 2b), with SEM and energy-dispersive X-ray (EDX) analysis detecting an accumulation of carbon (C), nitrogen (N), zinc (Zn), and oxygen (O). The surface morphology of LI ZIF-8 is quite different from the rhombohedral-shaped structures of the pristine material (see ref. [29] or TEM results in Figure 2). Notably, the EDX analysis post-laser exposure showed a decrease of nitrogen to negligible levels and a marked increase in oxygen content, rising to 26.1%. This change was higher in the flatland regions of LI ZIF-8 (Figure 2c), where the mesoporous structures displayed a homogeneous distribution of C, N, Zn, and O.

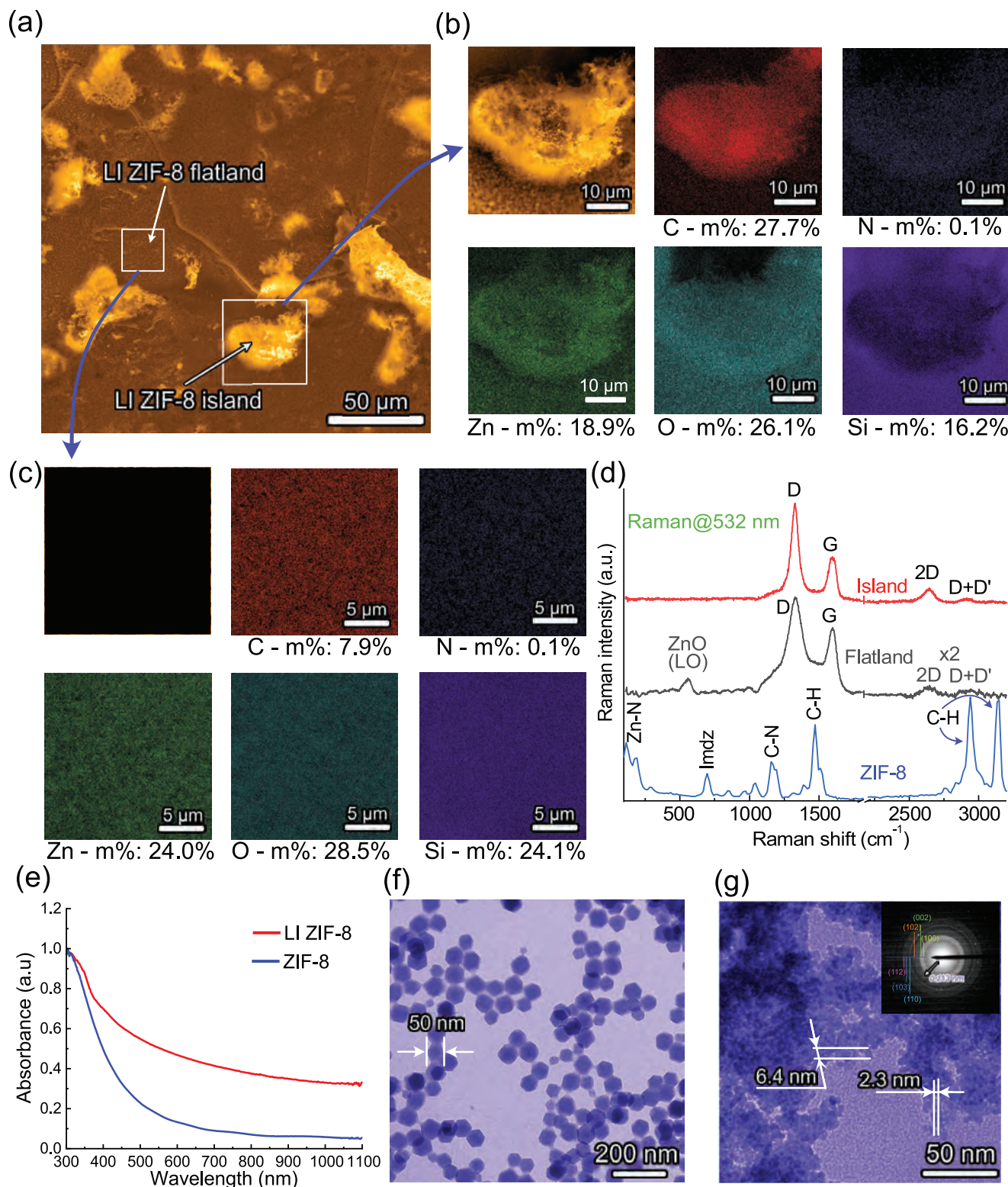


Figure 2. ZIF-8 on glass substrate for large-area irradiation. a) SEM image of LI ZIF-8. b) SEM image of LI ZIF-8 island. c) SEM image of the microporous flat-land-like area with elemental distributions. d) Raman spectra of LI ZIF-8 island and the microporous flat-land-like area (the Raman spectra were recorded at spots with low PL intensity). e) UV-vis spectra of LI ZIF-8 and ZIF-8. f) TEM image of ZIF-8 before laser irradiation, showing the uniform rhombic dodecahedron crystals of ZIF-8. g) TEM image of LI ZIF-8, confirming the nanostructure formation, aligning with the average crystal size estimated from XRD data (inset: selected area electron diffraction of LI ZIF-8).

Raman spectroscopy results further elucidated the structural evolution induced by the laser process (Figure 2d). Before laser irradiation, we observed characteristic ZIF-8 peaks at 174 and 697 cm^{-1} related to Zn–N coordination and imidazole ring vibrations,^[30,31] alongside other peaks associated with C–H and C–N vibrations.^[31] Post-irradiation, these initial peaks were replaced by the D (≈ 1350), G (≈ 1580), and 2D ($\approx 2700 \text{ cm}^{-1}$) bands, indicative of carbon formation. A single Lorentz peak fit of the 2D band suggested the presence of graphene^[32] or turbostratic graphite, similar to decoupled graphene layers. In the flatland-like areas of LI ZIF-8, broad D and G peaks were observed alongside a low-intensity 2D peak. We also observed a broad peak at 561 cm^{-1} , attributed to the LO ZnO mode reported under resonance conditions or charge transfer effects.^[33] We tentatively attribute the appearance of this LO peak to charge transfer between defected ZnO and carbon quantum dots, which could also explain the material's strong luminescence even when excited below ZnO's bandgap. This contrasted with the island-like LI ZIF-8 that did not show the ZnO peak at 561 cm^{-1} , and instead, sharper D and G peaks with a higher 2D peak intensity were observed.

Figure 2e shows the UV–vis spectra of LI ZIF-8 and ZIF-8. The increase in absorption close to 300 nm is related to the $n\text{-}\pi^*$ transition of the conjugated C=O or C–O bonds.^[34] TEM imaging results in Figure 2f corroborated the rhombic dodecahedron morphology of pristine ZIF-8, with an average particle size of 50 nm. Post-laser treatment, LI ZIF-8 showed the appearance of nanostructures with sizes between 2.3 and 6.4 nm (Figure 2g). The selected area electron diffraction pattern in the inset in Figure 2g showed the crystal lattices of (100), (002), and (102), consistent with ZnO.^[35] In addition, we also observe the d-space lattice of 0.213 nm, related to the (100) lattice of graphene.^[36]

The (XRD) spectrum of pristine ZIF-8, as illustrated in Figure 3a, displays prominent peaks at two-theta (2θ) values of 10.4°, 12.7°, 14.7°, 16.4°, and 18°. These peaks correspond to the (200), (211), (220), (310), and (222) crystal planes of ZIF-8,^[37] confirming the synthesis of highly crystalline structures.^[38] After laser irradiation, the XRD pattern changes drastically, the ZIF-8's characteristic peaks disappear, and a broad peak $\approx 25.5^\circ$ arises due to lattice disorder attributed to the presence of oxygen groups.^[39] This formation of nanocarbons is in agreement with the observations of Raman 2D, D, and G peaks. Utilizing the Scherrer equation, the average crystal size is estimated at 6.7 nm, matching graphene quantum dots dimensions previously reported^[40] and our direct TEM observations in Figure 2g.

Fourier-transform infrared spectroscopy (FTIR) provides further insights into the chemical transformations of ZIF-8 due to laser irradiation (Figure 3b). Before irradiation, distinct peaks at 1583 cm^{-1} and within the 1350–1500 cm^{-1} range are attributed to the C=N stretch and imidazole ring stretch of the ZIF-8 framework.^[41] Laser treatment results in the disappearance of these bands, with a new prominent peak at 2218 cm^{-1} emerging, likely associated with nitrile (CN) stretching.^[42] This modification suggests the formation of nitrogen-doped graphene, likely from the thermal decomposition of Zn–N bonds in the imidazole linker.

XPS analysis was conducted to elucidate the chemical changes in LI ZIF-8 at varying laser powers from 0.48 to 0.96 W, as shown in Figure 3c. Notably, C1s and N1s peak intensities decreased with increased laser power, whereas the O1s intensity increased.

Initial atomic ratios of C, N, O, and Zn were observed at 63.0%, 28.2%, 2.1%, and 6.7%, respectively, with oxygen presence due to the laser process being carried in air conditions (Figure 3d). Laser irradiation at 0.48 W resulted in a decrease of carbon to 58.6%, and nitrogen to 15.7%, while oxygen increased to 16.1%, and zinc to 9.3%. Higher laser powers further reduce carbon and nitrogen content while increasing oxygen and zinc levels.

High-resolution XPS spectra for individual elements, depicted in Figure 3e–h, reveal significant findings. The high-resolution C 1s spectrum of ZIF-8 exhibits peaks for C=C, C–C or C–H, and C–N bonds, with a small C=O peak and no evidence of sp^2 -hybridized carbon allotrope (Figure S6, Supporting Information). Post-irradiation, there is a marked rise in the C=O bond peak at 288.3 eV, suggestive of carboxyl groups in the nanocarbon structure, akin to graphene oxide. Nitrogen and C–N bonding are still detectable, indicating N-doped graphene formation, which is known to widen the bandgap and enhance PL emission in graphene quantum dots.^[27,43] The presence of sp^2 bonds in the C 1s spectrum suggests the formation of graphene-like materials after laser processing of ZIF-8. There was no significant change except a shift in the N 1s spectrum, which could be related to the change in C–N bonding from 2-methylimidazole to N-doped graphene. The O 1s signal after laser treatment increased notably, indicating a significant incorporation of oxygen into the sample. The C–O, C=O peaks observed in the O 1s spectrum are in good agreement with the C 1s spectrum. Additionally, the appearance of the Zn–O peak in the O 1s spectrum suggests ZnO formation due to laser treatment. The Zn-2p spectrum displayed a doublet at ≈ 1022 and 1045 eV, corresponding to the Zn- $2p_{3/2}$ and $2p_{1/2}$ core levels (Figure 3f). The first peak is related to Zn $^{2+}$ ions in an oxygen-deficient ZnO matrix.^[44] The sharp Zn- $2p_{3/2}$ peak relates to the formation of Zn $^{2+}$ on the sample surface.^[45] Laser power increase also induces a blue shift in Zn 2p binding energy, potentially signaling ZnO formation (Figure 3f). The intensity of O 1s increased with the increase of laser power (Figure 3g), which demonstrated the rise in oxygen content and possible formation of functional groups on the carbon surface or ZnO. Shifts in N 1s spectra correspond to increasing C–N bond proportions within LI ZIF-8 (Figure 3h). Collectively, the Raman, XRD, FTIR, SEM, and TEM analyses support the transformation of ZIF-8 into N-doped nanocarbons and ZnO through laser processing, highlighting the potential for new applications of these modified materials.

Elucidating the mechanism responsible for the remarkable 70-fold increase in PL is essential for understanding the laser-driven conversion of ZIF-8 into nitrogen-doped nanocarbons. During PL emission, the material absorbs and re-emits photons, a phenomenon prominently observed in carbon-based nanomaterials due to numerous pathways enabling the radiative recombination of excited electron–hole pairs.^[46] In the case of graphene quantum dots (GQDs), the PL is predominantly influenced by quantum confinement effects and edge defects.^[47]

Quantum confinement comes into play at the nanoscale, typically below 10 nm, where quantum mechanical effects dictate electronic properties. This confinement effect discretizes the electronic band structure, allowing for the direct recombination of electron–hole pairs, resulting in light emission at discrete wavelengths.^[48] A reduction in GQD size correlates with an increase in PL intensity and a red-shift in emission,^[49] which

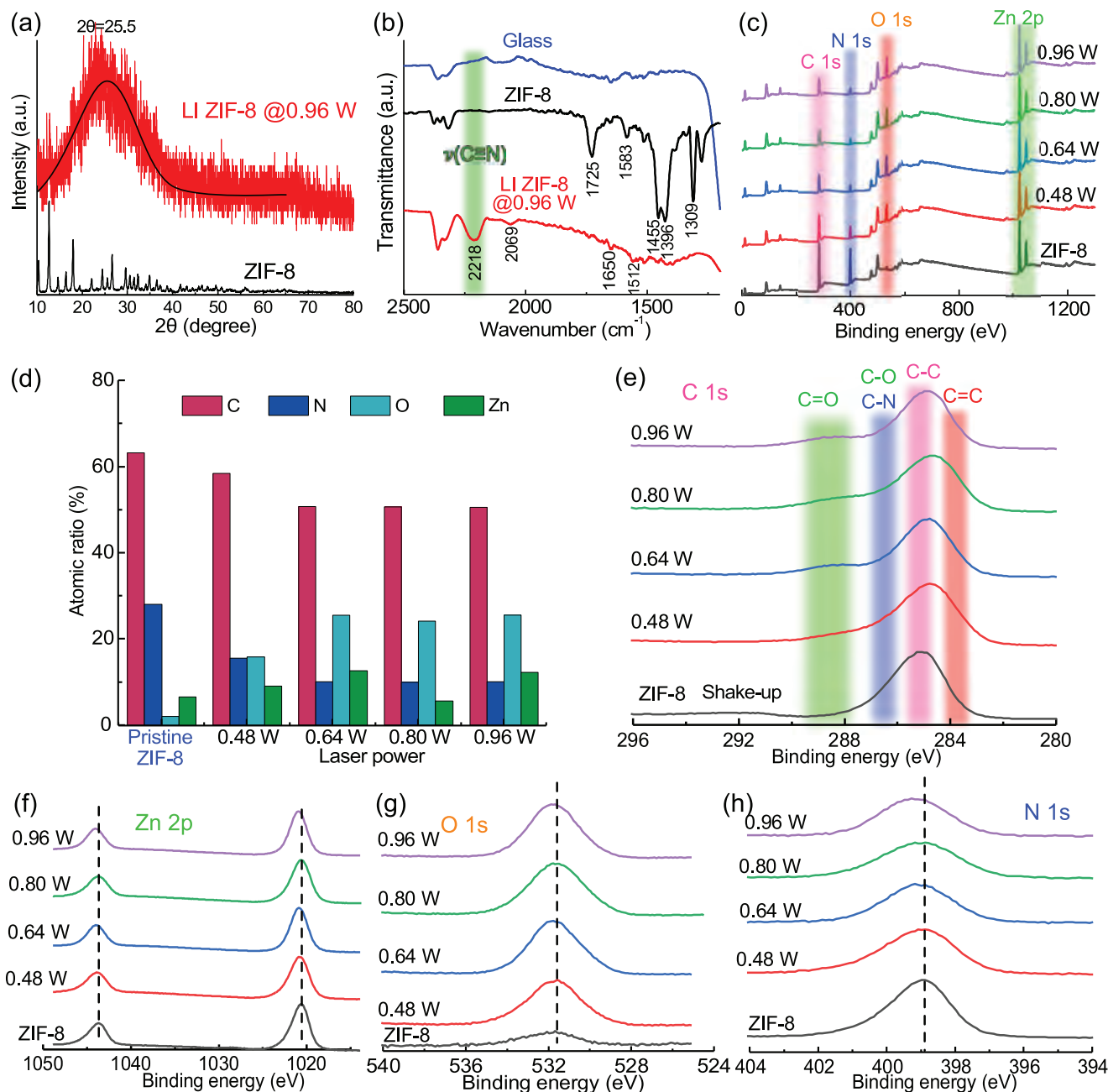


Figure 3. ZIF-8 on glass substrate for large-area irradiation by a laser engraver. a) XRD spectrum of ZIF-8 and LI ZIF-8. b) FTIR spectra of glass, ZIF-8 before and after laser treatment. c) Survey spectra of ZIF-8 and LI ZIF-8, irradiated by laser engraver at different laser power: 0.48, 0.64, 0.8, and 0.96 W. d) Atomic ratio of C, N, O, and Zn elements, obtained from XPS results, high-resolution. XPS results of e) C 1s, f) Zn 2p, g) O 1s, h) N 1s of LI ZIF-8 at different laser power.

aligns with our observations of PL red-shifting near the ablated spot's center, indicative of diminishing particle size and supporting the quantum confinement model.^[50] The crystalline dimensions estimated at 6.7 nm for our LI-ZIF-8 also fit within the expected range for quantum confinement in GQDs.^[51]

Edge defects, distinct from quantum confinement, introduce emissive states through altered bond hybridization and irregularities in the graphene lattice. These defects are known to facilitate radiative recombination by trapping excited charge carriers

at intermediate energy states. Notably, while defects on the basal plane tend to quench fluorescence, edge defects can significantly amplify PL.^[52]

Nitrogen doping modifies the emissive properties of graphene by introducing mid-gap energy states. Selective edge N-doping, as opposed to center doping, is particularly effective in enhancing fluorescence by modifying the energies of excited states and increasing the likelihood of radiative transitions. The spectral shifts in PL are influenced by how nitrogen dopants hybridize with

the graphene edge—symmetrical hybridization can cause a blue shift, while asymmetrical hybridization leads to a red shift.^[53] Given that ZIF-8 inherently contains nitrogen within its imidazole linkers, laser irradiation could facilitate the migration of nitrogen atoms to the edges of the newly formed GQDs, potentially enhancing PL through dopant effects and quantum confinement.

Graphene oxide's diverse functional groups (COOH, OH, C—O—C, C=C, C=O) create a complex interplay between sp^2 and sp^3 hybridized carbon, allowing for tunability of the electronic structure.^[54] This tunability can induce specific electronic transitions such as $\sigma \rightarrow n$, $n \rightarrow \pi^*$, and $\pi^* \rightarrow \pi$, modulating the PL spectrum.^[55] Furthermore, Liu *et al.* demonstrated that manipulating intrinsic states in highly crystalline structures and defect states associated with oxygen functional groups can control blue and green PL emissions in GO quantum dots.^[27]

In light of these findings, it is apparent that multiple structural and electronic factors influence PL behavior in nanocarbon systems. Consequently, we characterize the resulting system as N-doped nanocarbon, which is a direct product of the laser-induced carbonization process of ZIF-8.

2.3. Elucidating the Mechanism Behind the Laser Integration of ZIF-8 into TPU

Building on the results discussed above, showing that laser irradiation can provide high photoluminescence absent in the pristine ZIF-8 by producing N-doped nanocarbons, we ventured into integrating these luminescent units into flexible substrates. This step is critical in flexible electronics, especially for wearables and IoT sensors, where novel photoluminescent composites developed through eco-friendly methods are highly sought after. Thermoplastic polyurethane (TPU), known for its biocompatibility, elasticity, and medical application suitability,^[56,57] was chosen as the substrate. We applied 450 nm laser irradiation to ZIF-8 coated on 3D printed TPU substrates, forming a composite called LI ZIF-8/TPU. The choice of ZIF-8, with its strong absorption at 450 nm, facilitated effective composite formation at an optimal laser power of 0.64 W.

To explore the incorporation of nitrogen-doped nanocarbons and ZnO nanoparticles into TPU, we performed SEM analyses on cross-sections of LI ZIF-8 on TPU. The SEM images (Figure 4a,b) distinctly show the integration of ZnO and N-doped nanocarbons within the TPU matrix, indicating the successful composite formation. A noticeable feature in these images is the presence of cavities within the LI ZIF-8/TPU composite, resulting from the porous structure created by laser treatment.

The laser integration of ZIF-8 into the TPU matrix is facilitated by the strong absorption of ZIF-8 at the 450 nm laser wavelength. Upon laser irradiation, ZIF-8 likely undergoes photochemical and photothermal processes that induce structural and chemical changes. Specifically, the laser treatment leads to the decomposition of the organic linkers in ZIF-8, forming nitrogen-doped nanocarbons. Additionally, the metal nodes (Zn^{2+}) in ZIF-8 are converted into ZnO nanoparticles. These species act as nucleation sites and promote the intermixing and embedding within the TPU polymer chain. The high temperatures and localized

heating caused by the laser irradiation facilitate their diffusion and incorporation into the TPU matrix.

The cavities observed in the SEM images of the LI ZIF-8/TPU composite arise from the decomposition of ZIF-8's organic linkers and partial melting of the TPU surface contacting the ZIF-8 film during laser irradiation. This induces the engulfment of the ZIF-8 species by the melted TPU, akin to the process reported by Rodriguez *et al.* 2021^[58] for nanoparticle integration into polymers via laser treatment. These cavities can enhance the surface area and provide pathways for mass transport by the interconnected network of cavities.

(EDX) elemental mapping of the composite (Figure 4b) further elucidates the distribution of elements within the material. Remarkably, zinc was found not only on the surface layers directly affected by the laser but also extended $\approx 46 \mu\text{m}$ into the depth of the TPU substrate. This observation indicates a significant diffusion of ZIF-8 decomposition products deeper into the substrate, likely due to the localized heat generated during the laser integration process, as recently reported in the laser processing of graphene oxide films on thermoplastic polymers.^[59]

In contrast to zinc, the distribution of nitrogen, as revealed by the elemental mapping, was predominantly concentrated in areas characteristic of the TPU matrix. This distribution aligns with the expected C—N bonding in TPU's chemical structure and reflects the previously discussed reduction in nitrogen content following laser treatment. The proximity of oxygen to areas containing zinc hints at the formation of ZnO, likely a byproduct of the interaction between ZIF-8 and the ambient environment during the laser treatment process.

The dominant presence of carbon, constituting 67.1% of the mass ratio, is in line with expectations, considering carbon is a primary constituent in both TPU and ZIF-8. This high carbon content further confirms the effective integration of ZIF-8-derived materials into the TPU substrate, highlighting the success of the laser-assisted composite formation process.

Upon examining the surface morphology of the LI ZIF-8/TPU composite through SEM and EDX analyses (Figure 4c,d), a unique dual morphology becomes evident despite the overall uniform integration. This morphology is characterized by island-like regions and highly porous, foam-like structures. The boundaries of these island-like areas of LI ZIF-8 are sensitive to different photon fluxes, with the distance between these domains increasing with the laser power. This phenomenon is likely attributable to the localized melting of the TPU under high temperatures, leading to the encapsulation of LI ZIF-8 regions, a process similar to that observed in graphene oxide (GO) systems.^[59]

Elemental mapping conducted post-irradiation supports this hypothesis. It reveals that zinc (Zn) is evenly distributed across the composite's flat and island-like regions (Figure 4d), suggesting uniform material diffusion during the laser treatment. In contrast, carbon (C) is predominantly found in the porous areas, reflecting the carbonization of ZIF-8 within these zones. This distribution pattern indicates the successful incorporation of ZIF-8-derived materials into the TPU matrix. An interesting aspect of the LI ZIF-8/TPU composite is its porous architecture, which features thin graphene walls (Figure 4e–g). This structure was not observed in LI ZIF-8 when applied to glass substrates, implying that the type of substrate can influence the resulting morphology of LI ZIF-8, possibly due to variations in local temperature during

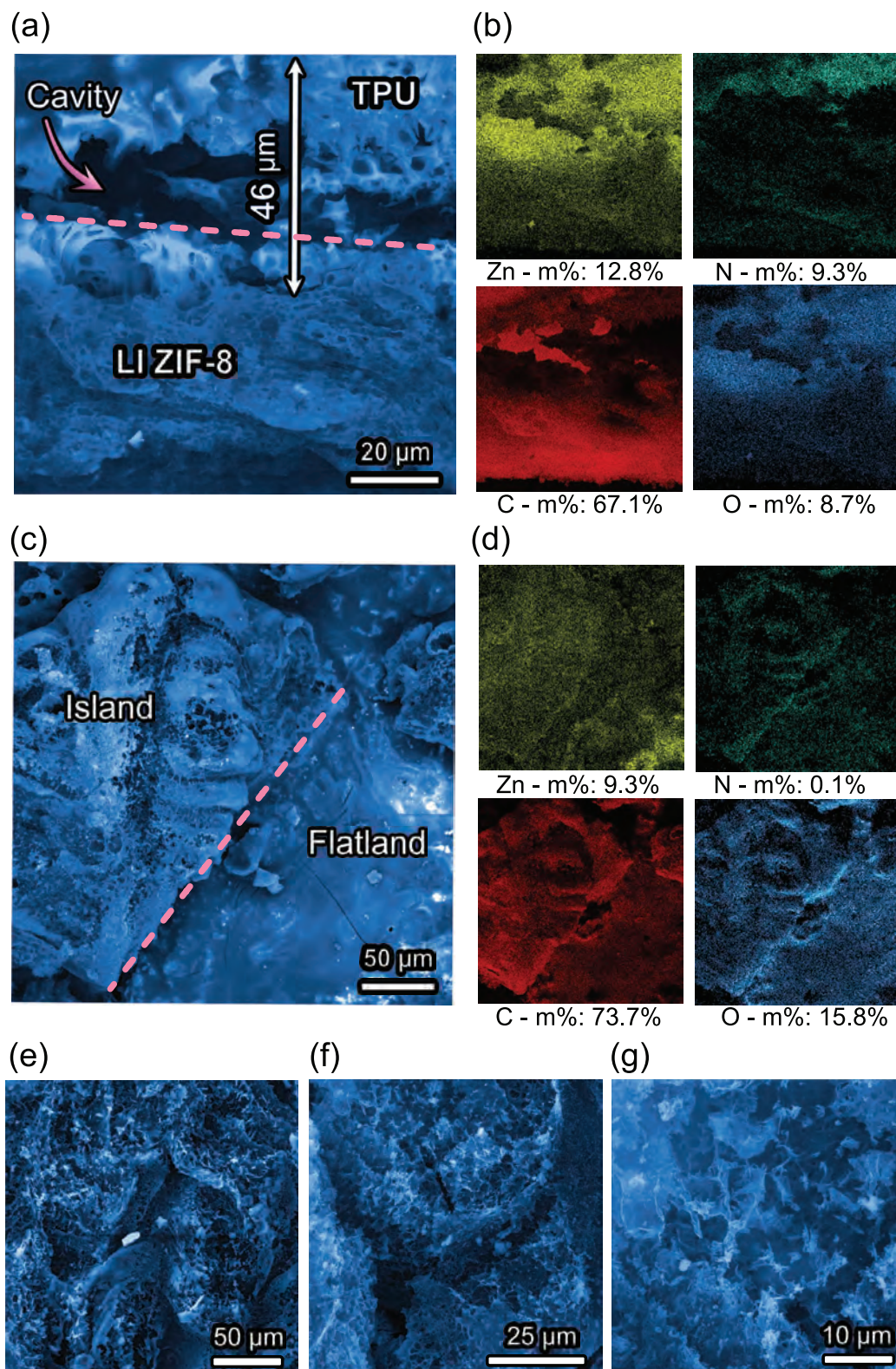


Figure 4. Morphological and compositional characterization of LI ZIF-8/TPU composite. a) Cross-sectional SEM image. b) Element distribution in Figure 4a and their portion in mass. c) SEM images. d) Element distribution in 4c and their portion in mass. e–g) High-magnification SEM images of the porous architecture reveal thin graphene walls.

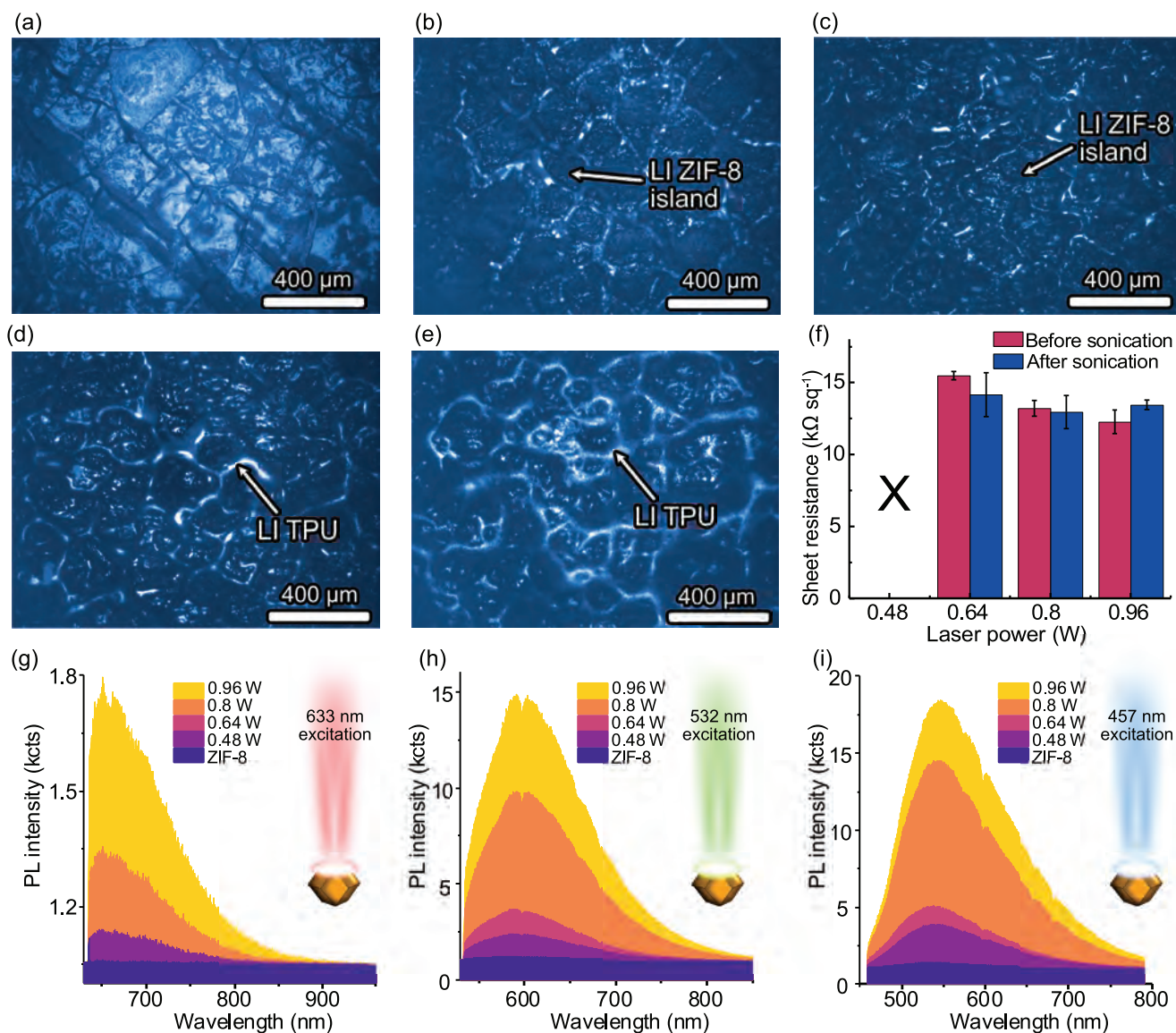


Figure 5. Laser power effects on morphology and PL of LI ZIF-8/TPU composite. a) Optical image of ZIF-8 on TPU. Composite formation b) at 0.48 W minimal porous domains. c) at 0.64 W increased porous domains. d) at 0.8 W extensive porous foam-like domains. e) at 0.96 W predominant porous foam-like domains. f) The sheet resistance of LI ZIF-8/TPU irradiated by different laser power before and after sonication. PL spectra of LI ZIF-8/TPU excited by g) 633 nm, h) 532 nm, and i) 457 nm lasers.

the laser treatment. The LI ZIF-8/TPU structure we achieved resembles those obtained through laser-induced graphene formation in other polymers.^[60] To further characterize the composite, we conducted XRD, IR, and UV-vis spectroscopic analyses on the LI ZIF-8/TPU irradiated at this specific laser power. However, distinguishing the signals of LI ZIF-8/TPU from those of the TPU substrate proved challenging due to the dominance of the latter's signal in the collected data (Figure S7, Supporting Information).

To investigate how different laser power settings affect the morphology of the laser-irradiated ZIF-8/TPU (LI ZIF-8/TPU) composite, we employed a range of laser powers from 0.48 to 0.96 W for irradiating ZIF-8 on TPU. The resulting morphological changes are presented in Figure 5a–e. Initially, ZIF-8 nanopar-

ticles were drop-cast onto the TPU substrate, forming distinct domains separated by cracks (Figure 5a). As the laser power increased, these areas progressively darkened, indicating ZIF-8 carbonization (Figure 5b,c). Notably, the extent of flatland-like LI ZIF-8 regions expanded with higher laser powers, aligning with the heat accumulation-induced melting hypothesis for border formation (Figure 5d,e). This behavior was similar to that observed in the laser treatment of ZIF-8 on glass substrates. As we see in Figure S8a (Supporting Information), ZIF-8 aggregates on glass, which leads to uneven distribution. When ZIF-8 is laser irradiated, the LI ZIF-8 island appears at a power of 0.48 mW, and the distance between LI ZIF-8 islands is larger than between ZIF-8 islands (see Figure S8a,b, Supporting Information). As the laser power increases, the size of the LI

ZIF-8 island becomes smaller, as shown in Figure S8b–e (Supporting Information). Optical images of LI ZIF-8 and its PL map in the irradiated area and at the edge of the irradiated area are illustrated in Figure S8f–i (Supporting Information). The crack of ZIF-8 expands from the unirradiated to the irradiated region (see Figure S8g, Supporting Information), which shows the sensitivity of the island edge and demonstrates the ablation could start at the edge of the ZIF-8 island. We propose that the edge of the ZIF-8 island's sensitivity to laser light, combined with its uneven distribution, potentially contributes to inhomogeneity in the distribution of the LI ZIF-8 regions. Figure S8f (Supporting Information) shows the optical image of LI ZIF-8, irradiated by a laser power of 0.48 W, and its PL intensity map. Although the LI ZIF-8 PL distribution is inhomogeneous—the PL at the island is low at the bottom-center of the PL map area marked by an arrow—the PL of the area around this island is characterized by high intensity. Consequently, the uneven distribution of ZIF-8 could be one of the reasons for the inhomogeneous distribution of PL in the LI ZIF-8 sample. At the edge of the irradiated area, we even observed stronger PL intensity, additionally supporting our conclusions on the PL enhancement at the edge of ablated ZIF-8 (see Figure S8g–i, Supporting Information).

In terms of functional characteristics, particularly the electrical properties crucial for flexible electronic devices, we observed that the LI ZIF-8/TPU composite attained electrical conductivity at laser powers above 0.64 W. This conductivity remained stable even after subjecting the material to an ultrasonication bath, suggesting robust interfacial integrity and mechanical durability (Figure 5f). Additionally, laser processing transformed ZIF-8 into strong luminescent nanocarbons within the TPU matrix. As discussed earlier, the strong luminescence could originate from the presence of N-doped nanocarbons, the formation of ZnO nanoparticles and/or the laser treatment of TPU. The optical images and Raman spectrum showed the presence of TPU and its ablation by laser irradiation (Figure S9a–c, Supporting Information). Time-dependent PL measurements at higher power settings confirmed the increase of PL signal while irradiation (Figure S9d, Supporting Information). Specifically, the PL intensity of the TPU surface increased tenfold under laser irradiation compared to its non-irradiated state (Figure S9e, Supporting Information), suggesting that both N-doped nanocarbons and laser-treated TPU contribute to transforming ZIF-8 films into porous, N-doped carbon nanostructures exhibiting strong PL over an extensive surface area.

Further PL analysis of LI ZIF-8/TPU revealed that the flat regions of the composite emitted PL were three times stronger than the porous areas (as shown in Figure S10, Supporting Information). When the excitation laser wavelength for LI ZIF-8/TPU was reduced, a significant increase in PL peak intensity was observed, along with a blue shift in the peak emission position (Figure 5g–i).

These excitation-dependent PL emission characteristics strongly support the presence of nanocarbons on the composite's surface, as many works have reported the steady redshift in PL emission and decrease of PL intensity in the increase of excitation wavelength.^[61–63] Furthermore, an increase in the laser power used to create LI ZIF-8/TPU led to a marked rise in PL emission intensity, reinforcing the idea that laser irradiation

of TPU itself also contributes to enhanced PL observed in the composite.

2.4. Temperature Sensors

We further explored their temperature-responsive PL characteristics by leveraging the laser-induced transformation of ZIF-8 into nitrogen-doped nanocarbons exhibiting high PL emission. Utilizing excitation wavelengths of 457 and 532 nm, we conducted a detailed analysis of the PL response to temperature changes. A heating stage enabled precise temperature control, varying from 25 to 45 °C in 2 °C increments, mirroring typical human body temperature ranges. The PL spectrum was meticulously recorded at each temperature step using a Raman system.

Our findings revealed a notable decrease in PL intensity at 530 and 600 nm wavelengths as the temperature increased for both excitation wavelengths (Figure 6a–d). This decrease is likely due to the thermal activation of nonradiative decay channels and relaxation processes.^[64] The observed linear reduction in PL intensity with rising temperature demonstrates the potential of these nanocarbon structures as nanoscale temperature sensors, which are particularly relevant for health monitoring applications.

Figure 6b,d shows the correlation between integrated PL intensity and temperature for 457 and 532 nm, respectively.

The relationship between integrated PL intensity and temperature for each excitation laser wavelength was formulated into linear equations as follows:

- For 457 nm excitation laser: $I(T) = -1.76 \cdot 10^4 T + 5.05 \cdot 10^6$, $R^2 = 0.9368$

Absolute sensitivity S and the relative sensitivity S_R is calculated by the formulas^[65]

$$S = \frac{d(I(T)/I(0))}{dT} \quad S_R = S \frac{I(0)}{I(T)} \quad (1)$$

where $I(T)$ is the integrated PL intensity at temperature T and $I(0)$ is the integrated PL intensity at room temperature.

- For 532 nm excitation laser: $I(T) = -4.1 \cdot 10^4 T + 3.4 \cdot 10^6$, $R^2 = 0.9196$

Here I represents the PL intensity, T is the temperature (°C). The LI ZIF-8/TPU showed a good correlation between PL intensity and temperature, based on the high correlation coefficient $R^2 > 0.9$ in a small range of temperatures, which is suitable for devices on the human body. The S_r for 457 and 532 nm excitation wavelengths were 4.5% °C⁻¹ at 46 °C and 5.5% °C⁻¹ at 45 °C, respectively. These values were higher than temperature sensors based on MOFs, for instance, 0.52% °C⁻¹ at 80 °C for MOF-nanocomposites,^[66] 1.19% °C⁻¹ for Rh101@UiO-67 nanohybrids,^[67] and 1.05% °C⁻¹ for Tb_{0.999}Eu_{0.001}-complexes RE(BPDC)(Ad) (BPDC=biphenyl-4,4'-dicarboxylic acid, Ad=adenine) polymer thin films.^[68]

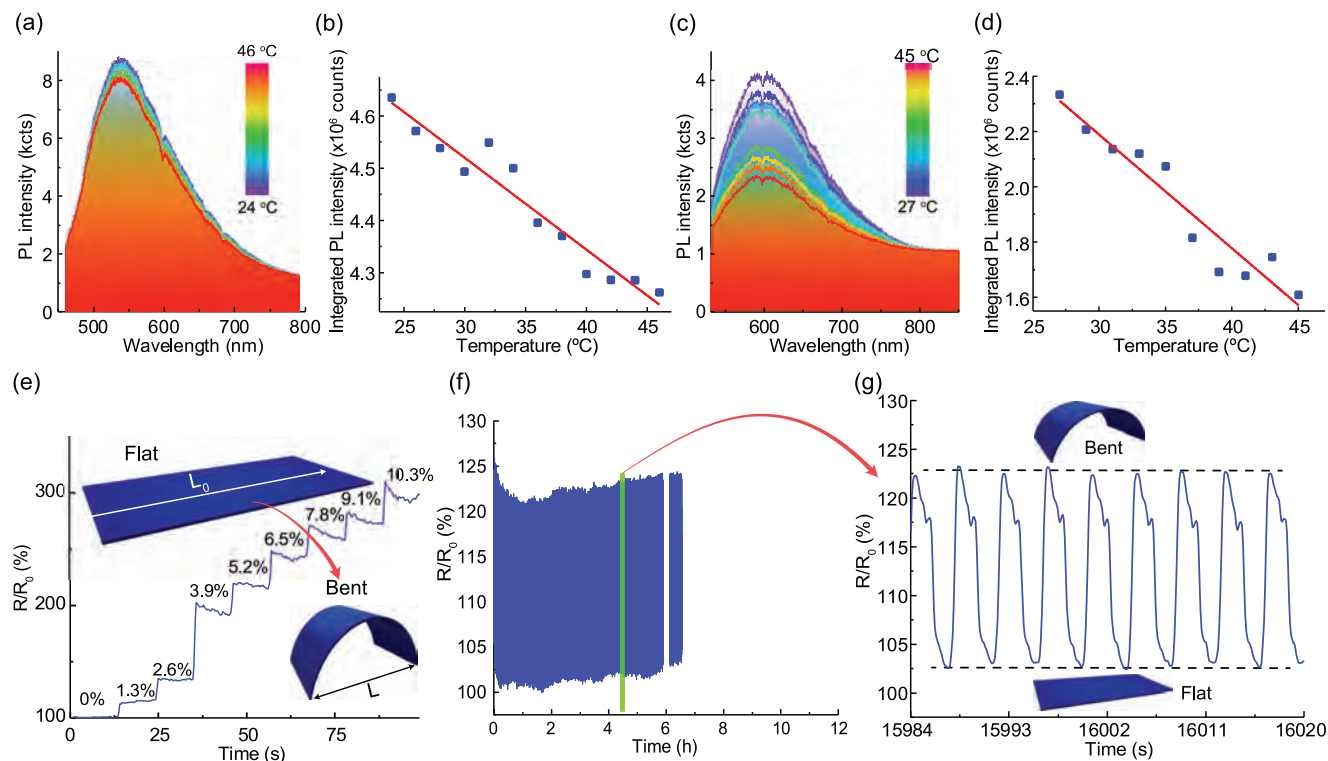


Figure 6. Applications of LI ZIF-8/TPU as temperature and bending sensor. a) Temperature-dependent PL of LI ZIF-8/TPU. b) Linear correlation of PL emission and the temperature with 457 nm laser excitation. c) Temperature-responsive PL emission of LI ZIF-8. d) Linear correlation of PL emission and the temperature with 532 nm laser excitation. e) Bending sensor at different deformations (inset: illustration of free and bent forms of LI ZIF-8/TPU electrode). f) Stability test of bending sensors. g) Stability test at small scale.

2.5. Bending Sensors

Multisensors allow us to reduce the number of devices required for complex applications. Moreover, flexible multisensors can adapt to human skin seamlessly and continuously register signals of interest related to critical health information.^[69] For human beings, bending is one of the most common movements. Therefore, flexible electronics that can track human motion have become a key research area in material sciences, device engineering, information technology, fitness, and biomedics.^[13,70,71] For instance, bending amplitudes and velocity can give us important information on physiological health, potentially related to conditions such as Parkinson's disease or rheumatism.^[72] Flexible sensors can measure the bending angle by direct and indirect measurements. While PL and many other physical effects were used to create deformation sensors,^[73–75] the piezoresistive effect remains the most widespread due to its simplicity and low cost. In this study, we selected the change in electrical resistance as the primary metric for evaluating bending sensor performance due to its direct correlation with strain^[76] and because it provides an independent measurement channel from PL intensity intended as the channel for temperature sensing. The ZIF-8 carbonization has the additional benefit of making it electrically conductive, which can be exploited to fabricate robust and reliable deformation sensors. To assess the electromechanical performance of the laser-irradiated ZIF-8/TPU (LI ZIF-8/TPU) electrode as a

potential bending sensor, we conducted a series of tests to measure its resistance under varying degrees of bending (Figure 6e). The methodology involved altering the distance between the two ends of the electrode and quantifying the deformation level (ΔL) using the formula: $\Delta L = (L_0 - L)/L_0 \times 100\%$, where L represents the distance between the electrode ends under bending, and L_0 is the initial distance when the electrode is in its relaxed state.

Our observations indicated that the electrode's resistance increased proportionally with the degree of deformation. Notably, at a deformation level of 3.9%, there was a pronounced spike in resistance attributed to the disruption of connectivity between the crystalline carbon layers in the LI ZIF-8/TPU structure at certain points. This threshold marked the limit of effective sensor performance under bending conditions.

For a comprehensive evaluation of mechanical endurance, the electrodes underwent repetitive bending cycles—10,000 times over 11 h. The results in Figure 6f,g demonstrated robust performance under these rigorous conditions. The resistance variation between the relaxed and bent states of the electrode is $\approx 20\%$ of the initial resistance (R_0), indicating a substantial signal-to-noise ratio. Such a characteristic is highly promising for applications in flexible electronics and wearable sensor technologies, where reliability under mechanical stress is paramount.

3. Conclusions

Laser processing of ZIF-8 led to a significant 70-fold increase in the PL intensity due to the formation of luminescent N-doped nanocarbons and ZnO nanoparticles under the influence of quantum confinement and edge defect effects. In addition, the temperature-dependent PL properties were analyzed at different excitation wavelengths. The results showed a linear decrease in PL intensity with increasing temperature. This observation demonstrates the potential of utilizing these laser-induced luminescent nanocarbons for nanoscale temperature sensing applications in health monitoring. Simultaneously, a key achievement of our study is the successful integration of nanocarbons into thermoplastic polyurethane (TPU), which yielded LI ZIF-8/TPU composites with impressive electromechanical properties that are well-suited for applications in flexible electronics and wearable sensors. The electrically conductive nature of LI ZIF-8/TPU was exploited in the design and fabrication of bending sensors. As a result, it was possible to achieve significant changes in resistance under deformation and to maintain stable characteristics even after 10,000 bending cycles, which emphasizes the durability of the electrodes. We hypothesize that future work will exploit the potential of the laser processing method to create arbitrarily shaped patterns of luminescent nanocarbons and ZnO nanoparticles derived from ZIF-8, with the subsequent goal of applying them to complex flexible electronic structures with unique PL characteristics.

4. Experimental Section

Preparation of ZIF-8 Powder: ZIF-8 was synthesized using the solvothermal method according to the procedure reported by Lee and coauthors.^[16] 480 mg of 2-methylimidazole and 240 mg of Zn(NO₃)₂·6H₂O were dissolved separately in 10 mL methanol. The two solutions were mixed and stirred for 1 h, resulting in the formation of ZIF-8 powder. The obtained ZIF-8 was isolated by centrifugation at 5000 rpm for over 10 min with subsequent washing by MeOH. The obtained powders were re-dispersed and stored in methanol to prevent agglomeration before usage.^[17]

Raman and Photoluminescence Spectroscopy: Raman and PL spectra were recorded by a confocal Raman microscope (NTEGRA Spectra, NT-MDT SI, Russia). The Raman microscope was configured with 633, 532, and 457 nm diode lasers. The laser beam was focused on the sample using 5×, 20×, and 100× Mitutoyo objectives. Samples were irradiated by different lasers to investigate the laser irradiation process, and the spectra were recorded over time. A grating with 150 grooves mm⁻¹ was used for PL experiments, while a 600 grooves mm⁻¹ grating was used for Raman experiments. Due to high PL, Raman signals can be recorded at some points with low PL.

Laser Processing of ZIF-8 in Large-Scale Manufacturing: ZIF-8 was deposited on a glass slide using the drop-casting method. For large-scale laser processing, the following procedure was used: Thermoplastic polyurethane (TPU) film was produced by 3D printer Ender-3 (Creality, China) from TPU filament from BestFilament (Russia). ZIF-8 was deposited on a 3D-printed TPU by drop-casting method. The laser process was conducted using a 450 nm wavelength computer-controlled laser diode modulated at 1.6 kHz. The laser power was controlled by the pulse duration.

A 120 W ultrasound bath with a frequency of 40 kHz was employed for the mechanical stability test.

Transmission Electron Microscopy (TEM): TEM images were recorded by Phillips CM12 transmission electron microscope (Phillips, Netherlands).

Scanning Electron Microscopy (SEM): SEM images and energy-dispersive X-ray (EDX) spectroscopy were obtained on Tescan Vega 3 SBH (TESCAN, Czech Republic).

X-Ray Diffraction (XRD): The XRD experimental data were obtained using a Shimadzu XRD-6000 diffractometer (Shimadzu, Japan) based on CuK α radiation with a sliding beam.

X-Ray Photoelectron Spectroscopy (XPS): Thermo Fisher Scientific XPS NEXSA spectrometer (Thermo Fisher Scientific, USA) with a monochromated Al K Alpha X-ray source working at 1486.6 eV was used for XPS. Survey spectra were recorded using radiation with an energy of 200 eV and an energy resolution of 1 eV. For the high-resolution spectra, pass energy was 50 eV, and energy resolution was equal to 0.1 eV. The spot area was 400 μm^2 . The flood gun was used for charge compensation. The XPS spectra were analyzed using the Advantage software. The XPS spectra were calibrated according to the C–C peak in the C 1s spectrum.

UV-Vis: Spectra were obtained using a UV-Vis spectrophotometer Agilent Cary 60 (Agilent Technologies, USA) in the 325–1100 nm region with a resolution of 2 nm.

Fourier-Transform Infrared Spectroscopy (FTIR): Spectra were recorded on IRAffinity-1S (Shimadzu, Japan), equipped with diamond crystal. Each measurement was done with 1500 scans with a resolution of 1 cm⁻¹.

4-Point Probe: The sheet resistance was retrieved on a 4-point probe station, MST-4000A (MS TECH, Korea), equipped with Potentiostat/Galvanostat P-45X (Electrochemical instruments, Russia). The probes were in a square arrangement at an equal distance of 1.5 mm. The current was set to 0.5 mA for 10 s. Sheet resistance was calculated by Equation 2:

$$R_{(s)} = \frac{2\pi}{\ln(2)} \times \frac{\Delta V}{I} = 9.06472 \frac{\Delta V}{I} \quad (2)$$

where: $R_{(s)}$: sheet resistance; ΔV : the change in voltage measured between the backside probes; I : the current applied between the inside probes.

Temperature Sensor Experiment: The temperature was controlled by a thermal heater integrated into a microscope setup NT-MDT Prima (NT-MDT, Russia).

Supporting Information

Supporting Information is available from the Wiley Online Library or from the author.

Acknowledgements

The authors acknowledge funding by Russian Science Foundation Grant No. 23-42-00081. R.W. thanks support from the National Natural Science Foundation of China (Grant No. 62261136551). Works related to SEM and EDX, TEM, and XRD were conducted using the equipment of the Tomsk Regional Core Shared Research Facilities Center of National Research Tomsk State University. The authors thank the central laboratories of Tomsk Polytechnic University (Analytical Center) for the XPS measurements. The authors thank Elizaveta Dogadina for her help with the scientific illustrations in this work. The authors acknowledge the help from R. Gulyaev in ZIF-8 synthesis and Andrey Averkiev for the simulation of laser processing of ZIF-8.

Conflict of Interest

The authors declare no conflict of interest.

Author Contributions

T.-H.T. developed a methodology, performed investigation, formal analysis, and visualization, and wrote the original draft, reviewed and edited

the final draft. A. G. developed methodology, performed investigation, formal analysis, and visualization, wrote the original draft, and reviewed and edited the final draft. D. K. developed methodology, performed investigation and formal analysis. P.S. P. developed methodology and reviewed and edited the final draft. R. W. performed conceptualization, acquired funds, reviewed and edited the final draft. R.D.R. performed visualization and formal analysis, wrote the original draft, reviewed and edited the final draft, and acquired funds. E.S. performed conceptualization and formal analysis, developed methodology, acquired funds, Wrote the original draft, and reviewed and edited the final draft.

Data Availability Statement

The data that support the findings of this study are available in the supplementary material of this article.

Keywords

bending sensor, laser fabrication, metal–organic framework, N-doped carbon nanocarbons, photoluminescence, temperature sensor

Received: July 3, 2024

Revised: August 1, 2024

Published online: August 31, 2024

- [1] Ö. Erdem, E. Derin, S. Zeibi Shirejini, K. Sagdic, E. G. Yilmaz, S. Yildiz, G. A. Akceoglu, F. Inci, *Adv. Mater. Technol.* **2022**, 7, 2100572.
- [2] R. Garg, F. Vitale, *MRS Bull.* **2023**, 48, 283.
- [3] C. Van Le, H. Yoon, *Int. J. Mol. Sci.* **2024**, 25, 1564.
- [4] H. Meskher, S. B. Belhaouari, F. Sharifianjazi, *Heliyon* **2023**, 9, e21621.
- [5] X. Chen, H. Gao, M. Yang, L. Xing, W. Dong, A. Li, H. Zheng, G. Wang, *Energy Storage Mater.* **2019**, 18, 349.
- [6] X. Lin, G. Gao, L. Zheng, Y. Chi, G. Chen, *Anal. Chem.* **2014**, 86, 1223.
- [7] Y. Wang, B. Wang, H. Shi, C. Zhang, C. Tao, J. Li, *Inorg. Chem. Front.* **2018**, 5, 2739.
- [8] L. Xu, G. Fang, J. Liu, M. Pan, R. Wang, S. Wang, *J. Mater. Chem. A Mater. Energy Sustain.* **2016**, 4, 15880.
- [9] R. Lin, S. Li, J. Wang, J. Xu, C. Xu, J. Wang, C. Li, Z. Li, *Inorg. Chem. Front.* **2018**, 5, 3170.
- [10] T. Wakaoka, K. Hirai, K. Murayama, Y. Takano, H. Takagi, S. Furukawa, S. Kitagawa, *J. Mater. Chem. C Mater. Opt. Electron. Devices* **2014**, 2, 7173.
- [11] Z. Chen, Z. G. Gu, W. Q. Fu, F. Wang, J. Zhang, *ACS Appl. Mater. Interfaces* **2016**, 8, 28737.
- [12] R. D. Rodriguez, S. Shchadenko, *Adv. Funct. Mater.* **2021**, 31, 1.
- [13] A. Lipovka, M. Fatkullin, S. Shchadenko, I. Petrov, A. Chernova, E. Plotnikov, V. Menzelintsev, S. Li, L. Qiu, C. Cheng, R. D. Rodriguez, E. Sheremet, *ACS Appl. Mater. Interfaces* **2023**, 15, 38946.
- [14] D. Kogolev, O. Semyonov, N. Metalnikova, M. Fatkullin, R. D. Rodriguez, P. Slepicka, Y. Yamauchi, O. Guselnikova, R. Boukherroub, *J. Mater. Chem. A Mater. Energy Sustain.* **2023**, 11, 1108.
- [15] Z. Lai, *Curr. Opin. Chem. Eng.* **2018**, 20, 78.
- [16] Y. R. Lee, M. S. Jang, H. Y. Cho, H. J. Kwon, S. Kim, W. S. Ahn, *Chem. Eng. J.* **2015**, 271, 276.
- [17] T. Peng Chee, U. S. Malaysia, O. Boon Seng, A. L. Ahmad, L. Siew Chun, U. S. Malaysia, U. S. Malaysia, U. S. Malaysia, *J. Physiol. Sci.* **2017**, 28, 215.
- [18] T. H. Tran, R. D. Rodriguez, N. E. Villa, S. Shchadenko, A. Averkiev, Y. Hou, T. Zhang, A. Matkovic, E. Sheremet, *J. Colloid Interface Sci.* **2023**, 654, 114.
- [19] Q. Lai, Y. Zhao, Y. Liang, J. He, J. Chen, *Adv. Funct. Mater.* **2016**, 26, 8334.
- [20] C. J. Youn, T. S. Jeong, M. S. Han, J. H. Kim, *J. Cryst. Growth* **2004**, 267, 526.
- [21] K. F. Lin, H. M. Cheng, H. C. Hsu, L. J. Lin, W. F. Hsieh, *Chem. Phys. Lett.* **2005**, 409, 208.
- [22] L. K. Jangir, Y. Kumari, A. Kumar, M. Kumar, K. Awasthi, *Mater. Chem. Front.* **2017**, 1, 1413.
- [23] A. Alkauskas, A. Pasquarello, *Phys. Rev. B Condens. Matter* **2011**, 84, 125206.
- [24] D. Reyes, M. Camacho, M. Camacho, M. Mayorga, D. Weathers, G. Salamo, Z. Wang, A. Neogi, *Nanoscale Res. Lett.* **2016**, 11, 424.
- [25] M. A. Sk, A. Ananthanarayanan, L. Huang, K. H. Lim, P. Chen, *J. Mater. Chem.* **2014**, 2, 6954.
- [26] S. Sarkar, M. Sudolská, M. Dubecký, C. J. Reckmeier, A. L. Rogach, R. Zbořil, M. Otyepka, *J. Phys. Chem. C* **2016**, 120, 1303.
- [27] F. Liu, M. H. Jang, H. D. Ha, J. H. Kim, Y. H. Cho, T. S. Seo, *Adv. Mater.* **2013**, 25, 3657.
- [28] B. Liu, J. Xie, H. Ma, X. Zhang, Y. Pan, J. Lv, H. Ge, N. Ren, H. Su, X. Xie, L. Huang, W. Huang, *Small* **2017**, 13, 1601001.
- [29] E. M. Mahdi, J. C. Tan, *Polymer* **2016**, 97, 31.
- [30] D. A. Carter, J. E. Pemberton, *J. Raman Spectrosc.* **1997**, 28, 939.
- [31] G. Kumari, K. Jayaramulu, T. K. Maji, C. Narayana, *J. Phys. Chem. A* **2013**, 117, 11006.
- [32] L. M. Malard, M. A. Pimenta, G. Dresselhaus, M. S. Dresselhaus, *Phys. Rep.* **2009**, 473, 51.
- [33] R. Cuscó, E. Alarcón-Lladó, J. Ibáñez, L. Artús, J. Jiménez, B. Wang, M. J. Callahan, *Phys. Rev. B Condens. Matter Mater. Phys.* **2007**, 75, 165202.
- [34] K. Zhang, Y. F. Ma, Y. Q. Zhang, H. Gao, Y. B. Han, *J. Lumin.* **2019**, 209, 116.
- [35] P. Jamdagni, P. Khatri, J. S. Rana, *Journal of King Saud University – Science* **2018**, 30, 168.
- [36] K. D. Esmeryan, C. E. Castano, A. H. Bressler, M. Abolghasemibizaki, C. P. Fergusson, A. Roberts, R. Mohammadi, *Diam. Relat. Mater.* **2017**, 75, 58.
- [37] K. Kida, M. Okita, K. Fujita, S. Tanaka, Y. Miyake, *CrystEngComm* **2013**, 15, 1794.
- [38] O. Shekhah, M. Eddaoudi, *Chem. Commun.* **2013**, 49, 10079.
- [39] V. Vatanpour, S. S. Mousavi Khadem, M. Masteri-Farahani, N. Mosleh, M. R. Ganjali, A. Badiie, E. Pourbashir, A. H. Mashhadzadeh, M. Tajammal Munir, G. Mahmodi, P. Zarrintaj, J. D. Ramsey, S. J. Kim, M. R. Saeb, *Journal of Water Process Engineering* **2020**, 38, 101652.
- [40] P. G. Balkanloo, K. M. Sharifi, A. P. Marjani, *Materials Advances* **2023**, 4, 4272.
- [41] Y. Hu, H. Kazemian, S. Rohani, Y. Huang, Y. Song, *Chem. Commun.* **2011**, 47, 12694.
- [42] G. Lee, D. Kossowska, J. Lim, S. Kim, H. Han, K. Kwak, M. Cho, *J. Phys. Chem. B* **2018**, 122, 4035.
- [43] D. Qu, M. Zheng, J. Li, Z. Xie, Z. Sun, *Light: Sci. Appl.* **2015**, 4, e364.
- [44] S. Y. Huang, Q. J. Cheng, S. Xu, D. Y. Wei, H. P. Zhou, J. D. Long, I. Levchenko, K. Ostrikov, *J. Appl. Phys.* **2012**, 111, 036101.
- [45] I. G. Morozov, O. V. Belousova, D. Ortega, M. K. Mafina, M. V. Kuznetsov, *J. Alloys Compd.* **2015**, 633, 237.
- [46] S. Zhu, Y. Song, X. Zhao, J. Shao, J. Zhang, B. Yang, *Nano Res.* **2015**, 8, 355.
- [47] L. Wang, S. J. Zhu, H. Y. Wang, Y. F. Wang, Y. W. Hao, J. H. Zhang, Q. D. Chen, Y. L. Zhang, W. Han, B. Yang, H. B. Sun, *Adv. Opt. Mater.* **2013**, 1, 264.
- [48] F. Yavari, C. Kritzinger, C. Gaire, L. Song, H. Gulapalli, T. Borca-Tasciuc, P. M. Ajayan, N. Koratkar, *Small* **2010**, 6, 2535.
- [49] Z. Liu, F. Li, Y. Luo, M. Li, G. Hu, X. Pu, T. Tang, J. Wen, X. Li, W. Li, *Molecules* **2021**, 26, 3922.

- [50] S. Zhu, Y. Song, J. Wang, H. Wan, Y. Zhang, Y. Ning, B. Yang, *Nano Today* **2017**, *13*, 10.
- [51] F. Libisch, C. Stampfer, J. Burgdörfer, *Phys. Rev. B Condens. Matter* **2009**, *79*, 115423.
- [52] R. Rabeya, S. Mahalingam, A. Manap, M. Satgunam, M. Akhtaruzzaman, C. H. Chia, *Int. J. Quantum Chem.* **2022**, *122*, e26900.
- [53] X. Niu, Y. Li, H. Shu, J. Wang, *Nanoscale* **2016**, *8*, 19376.
- [54] M. Li, S. K. Cushing, X. Zhou, S. Guo, N. Wu, *J. Mater. Chem.* **2012**, *22*, 23374.
- [55] P. Zheng, N. Wu, *Chem. Asian J.* **2017**, *12*, 2343.
- [56] A. C. de Leon, Q. Chen, N. B. Palaganas, J. O. Palaganas, J. Manapat, R. C. Advincula, *React. Funct. Polym.* **2016**, *103*, 141.
- [57] S. Basak, *J. Macromol. Sci. Part A Pure Appl. Chem.* **2021**, *58*, 579.
- [58] R. D. Rodriguez, S. Shchadenko, G. Murastov, A. Lipovka, M. Fatkullin, I. Petrov, T. H. Tran, A. Khalelov, M. Saqib, N. E. Villa, V. Bogoslovskiy, Y. Wang, C. G. Hu, A. Zinovyev, W. Sheng, J. J. Chen, I. Amin, E. Sheremet, *Adv. Funct. Mater.* **2021**, *31*, 2008818.
- [59] E. Abyzova, I. Petrov, I. Bril', D. Cheshev, A. Ivanov, M. Khomenko, A. Averkiev, M. Fatkullin, D. Kogolev, E. Bolbasov, A. Matkovic, J. J. Chen, R. D. Rodriguez, E. Sheremet, *Polymers* **2023**, *15*, 4622.
- [60] R. Ye, D. K. James, J. M. Tour, *Adv. Mater.* **2019**, *31*, 1803621.
- [61] D. Pan, J. Zhang, Z. Li, M. Wu, *Adv. Mater.* **2010**, *22*, 734.
- [62] A. B. Siddique, S. M. Hossain, A. K. Pramanick, M. Ray, *Nanoscale* **2021**, *13*, 16662.
- [63] S. K. Cushing, M. Li, F. Huang, N. Wu, *ACS Nano* **2014**, *8*, 1002.
- [64] J. Liu, X. Ren, Y. Yan, N. Wang, S. Wang, H. Zhang, J. Li, J. Yu, *Inorg. Chem. Front.* **2018**, *5*, 139.
- [65] D. Das, S. L. Shinde, K. K. Nanda, *ACS Appl. Mater. Interfaces* **2016**, *8*, 2181.
- [66] Y. Ding, Y. Lu, K. Yu, S. Wang, D. Zhao, B. Chen, *Adv. Opt. Mater.* **2021**, *9*, 2100945.
- [67] Y. Zhou, D. Zhang, J. Zeng, N. Gan, J. Cuan, *Talanta* **2018**, *181*, 410.
- [68] X. Shen, B. Yan, *Dalton Trans.* **2015**, *44*, 1875.
- [69] X. Wang, Z. Liu, T. Zhang, *Small* **2017**, *13*, 1602790.
- [70] L.-Y. Zhou, J.-Z. Fu, Q. Gao, P. Zhao, Y. He, *Adv. Funct. Mater.* **2020**, *30*, 1906683.
- [71] C. Deng, P. Gao, L. Lan, P. He, X. Zhao, W. Zheng, W. Chen, X. Zhong, Y. Wu, L. Liu, J. Peng, Y. Cao, *Adv. Funct. Mater.* **2019**, *29*, 1907151.
- [72] C. Li, D. Liu, C. Xu, Z. Wang, S. Shu, Z. Sun, W. Tang, Z. L. Wang, *Nat. Commun.* **2021**, *12*, 2950.
- [73] W. Xu, Y. Li, J. Shang, Y. Wang, L. Hou, Y. Liu, S. Qu, *Opt. Express* **2022**, *30*, 33136.
- [74] G. Saggio, F. Riillo, L. Sbernini, L. R. Quitadamo, *Smart Mater. Struct.* **2015**, *25*, 013001.
- [75] E. Biddiss, T. Chau, *Med. Eng. Phys.* **2006**, *28*, 568.
- [76] X. Zhang, D. Xiang, Y. Wu, E. Harkin-Jones, J. Shen, Y. Ye, W. Tan, J. Wang, P. Wang, C. Zhao, Y. Li, *Compos. Part A Appl. Sci. Manuf.* **2021**, *151*, 106665.